# The Earth's surface controls the depth-dependent seismic radiation of megathrust earthquakes

**Jiuxun Yin**[1], **Marine A. Denolle**[1,2]

[1]Department of Earth and Planetary Sciences, Harvard University
[2]Department of Earth and Space Sciences, University of Washington

**Key Points:**

- The frequency-depth dependence in the radiation of megathrust earthquakes is ubiquitous.
- Dynamic models suggest that earthquakes propagate as cracks updip and self-healing pulses downdip due to the Earth's surface and structures.
- The frequency-depth dependent radiation arises from this particular rupture behavior and thus is due to free-surface effects.

Corresponding author: Jiuxun Yin, jiuxun_yin@g.harvard.edu

## Abstract

Megathrust earthquakes exhibit a ubiquitous seismic radiation style: low-frequency seismic energy is efficiently emitted from the shallowest portion of the fault, whereas high-frequency seismic energy is efficiently emitted from the deepest part of the fault. Although most case-specific studies report this observation, we show that it is ubiquitous in global megathrust earthquakes between 1995 and 2021. Previous studies have interpreted this as an effect of systematic depth variation in either the plate interface frictional properties (Lay et al., 2012) or the P wavespeeds (Sallarès & Ranero, 2019). This work suggests an alternative hypothesis: the interaction between waves and ruptures due to the Earth's free surface and realistic structure is a leading and straightforward factor that can explain the observation. This hypothesis is supported by analyzing the seismic radiation generated in two-dimensional dynamic rupture simulations in realistic subduction zone models. We use a P wavespeed ($V_P$) model derived from a tomographic study. We create a density model using standard empirical relations with $V_P$ and an S wavespeed ($V_S$) model from realistic $V_P$ /$V_S$ ratio values reported by drilling and imaging studies. Our simulations show that the effects of free-surface reflections act on the fault to promote the propagation of crack updip. In contrast, the sharp material contrasts promote the self-healing of slip pulses downdip. The contrasting style in rupture thus explains the systematic depth variation in the source radiation's spectral content. We conclude that the subduction zone's realistic structure is necessary for better seismic and tsunami hazard assessment.


## Plain Language Summary

The largest earthquakes occur on the megathrusts of subduction zones and generate huge ground motions and devastating tsunami waves that threaten the coastal populations. Global databases of earthquake seismic signals reveal that almost all megathrust earthquakes have a particular radiation style. The shallow portion of the megathrust is where the seismic event generates tsunamis but low-frequency, less damaging ground motions, whereas deeper segments of the megathrust are where the rupture excites the high-frequency and destructive ground motion strongly felt by the nearby coastal and urban regions. The scientific community has focused on a depth dependence of fault-surface properties. This study instead shows that a dynamic feedback between seismic waves and rupture with the Earth's surface and realistic structures is sufficient to explain these observed phenomena.

## 1 Introduction

Some of the largest and most damaging earthquakes occur offshore in subduction zones: the Mw 9.4 1960 Great Chilean earthquake, the 1964 Mw 9.3 Great Alaskan earthquake, the Mw 9.2 2004 Sumatra earthquakes, and the Mw 9.0 2011 Tohoku-oki earthquake. Almost 1 in 10 people in the world live on the coast. Understanding the rupture behavior of megathrust earthquakes is critical for seismic and tsunami risk mitigation in coastal areas. The recent occurrence of multiple of these events has coincided with a vast expansion in seismic networks, which, in turn, has led to the discovery of a multitude of processes surrounding the rupture of these large earthquakes (Ishii et al. (2005); Lay et al. (2012), and references therein).

A remarkable observation of these earthquakes' seismic signature is that low-frequency (LF) seismic waves are mostly generated at the shallow, updip region, while high-frequency (HF) seismic waves tend to come from the deep, downdip part. We refer to this as the "depth-frequency relation" in this work. It is manifested in three ways. First, studies on earthquake source time functions highlight a shortening of the source pulse that is well explained by an increase in elastic properties with depth (Bilek & Lay, 1999; Houston, 2001; Vallée, 2013) and an increase in the relative contributions of high-frequency radiation at depth and along the megathrust (Ye et al., 2016; Chounet & Vallée, 2018). Second, the strong ground motions that are responsible for damaging urban infrastructure have been observed to originate from the downdip end of the megathrust (Kurahashi & Irikura, 2011; Asano & Iwata, 2012; Frankel, 2013). The third class of seismic observations is the back-projection (BP) image reconstructed from teleseismic P waves (Ishii et al., 2005). The BP image is a blurred representation of the slip history on the fault (Fukahata et al., 2014a; Yin & Denolle, 2019). Consequently, the images constructed at various frequency bands relate to the slip function's whole-event spectral content on the fault. Event-specific studies have shown that high frequencies are more efficiently generated at the downdip portion of the megathrust rather than its updip end (Kiser et al., 2011; Sufri et al., 2012; Yao et al., 2013; Melgar et al., 2016; Yin et al., 2016, 2017, 2018).

Here, we show three examples of such images for the Mw 9.0 2011 Tohoku-oki earthquake (D. Wang & Mori, 2011; Yao et al., 2011; Lay et al., 2012), the Mw 7.9 2015 Gorkha earthquake (Avouac et al., 2015; Yue et al., 2016; Yin et al., 2017), and the Mw 8.3 2015 Chilean Illapel earthquake (Melgar et al., 2016; Yin et al., 2016). We show both the low-frequency and high-frequency BP images in Fig. 1a - c. Supporting Information (Text S1, Figs. S1 - S3) provide additional information about data processing and results. These images clearly illustrate that HF source signals are emitted at greater depths than LF source signals.

We then turn to global databases of BP images provided by The Incorporated Research Institutions for Seismology (IRIS) over all the M6.5+ earthquakes since 1995 (Incorporated Research Institutions for Seismology Data Management Center, 2011). Here, we select 461 earthquakes between 1995 and 2021 within the latitude-longitude range of the available Slab2.0 plate interface model (Hayes et al., 2018). We then project each earthquake HF and LF BP image onto the slab model and calculate the HF and LF centroid depths. The centroid depth is a weighted average of the BP peak depths, the weights being the BP peaks. Finally, we select the 245 earthquakes that have a BP centroid depth shallower than 70 km. For most earthquakes, especially the large magnitude ones with a likelihood of better time and spatial resolution of the BP image, we find that the centroid depth of the HF BP peaks is systematically greater than that of the LF peaks (Fig. 1d and Fig. S4). Two events stand out as exceptions: the Mw 9.0 2011 Tohoku-oki earthquake (this is due to the choice in frequency bands, see Fig. 1a, or figures in Yao et al. (2011)) and the Mw 8.3 2006 Kuril Island earthquake (Ammon et al., 2008).

A common interpretation for these observations is the systematic depth variation in frictional properties that result from increasing temperature and pressure with depth and associated phase transformation of the minerals that compose the downgoing oceanic lithosphere. The argument is that systematic depth variations in fault properties can explain the evolution of the seismicity rates with depth (Scholz, 1998). It has also been widely used to explain the depth-varying seismic radiation of large megathrust earthquakes (Lay et al., 2012; Yao et al., 2013; Yin et al., 2017). Studies that simulate the dynamic rupture have adopted this with a parameterization of pre-stress or fault strength heterogeneity in the deeper portion of the seismogenic megathrust and have successfully reproduced HF and LF's relative contributions in seismic radiation (Huang et al., 2012; Galvez et al., 2014). A recent alternative interpretation is that the systematic increase in P wavespeed ($V_P$) with depth in subduction zones directly impacts the wavelength and frequency of seismic waves emitted at the source (Sallarès & Ranero, 2019). However, such an argument would also pertain to earthquakes from other tectonic environments, and such depth-dependence in radiation is neither observed in the continental nor oceanic lithosphere (Chounet & Vallée, 2018). Furthermore, we do not observe it for deeper earthquakes in the IRIS database (see Fig. S5).

Another major impact on megathrust earthquake dynamics is the asymmetrical fault-surface geometry: a shallow dipping fault intersects the Earth's free surface, and the accretionary and frontal wedge materials (hanging wall) are highly compliant com-

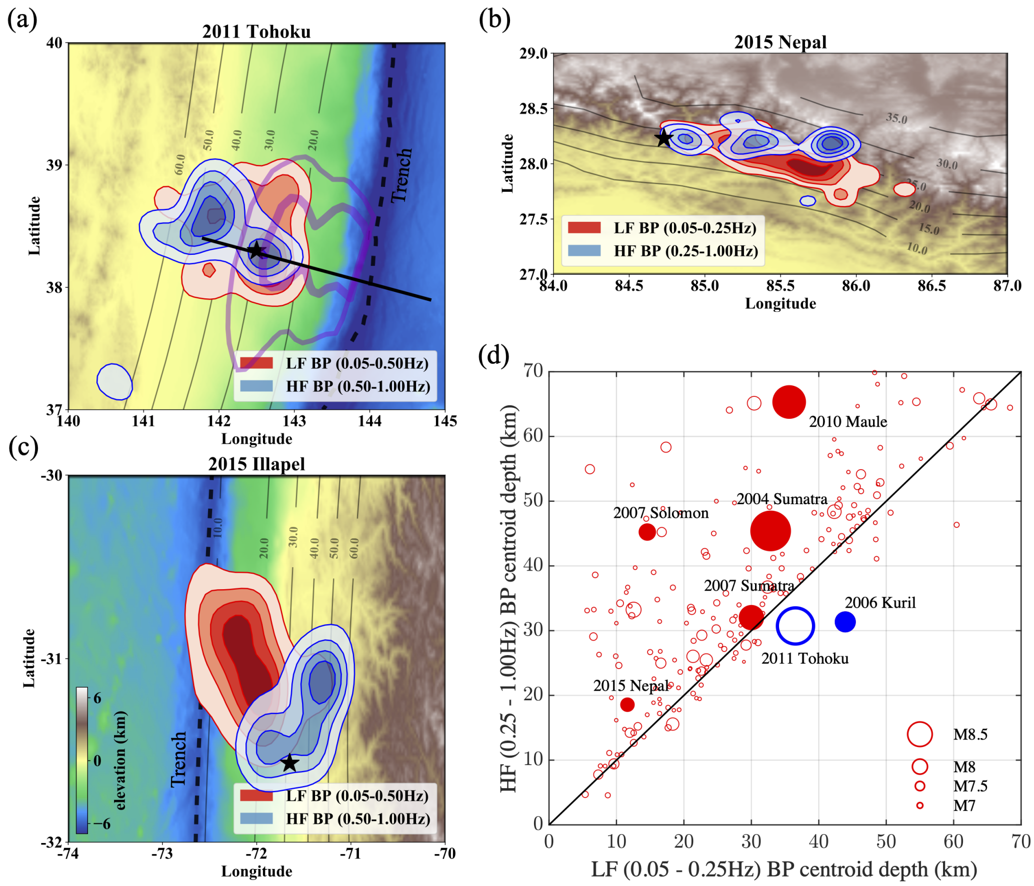


**Figure 1. Ubiquitous depth-frequency relation found by back-projection observations.** (a)-(c) BP images of the Mw 9.0 2011 Tohoku-oki, the Mw 7.9 2015 Gorkha, and the Mw 8.3 2015 Illapel earthquakes, respectively. The BP images are reconstructed using a high-resolution imCS-BP back-projection method we developed in Yin et al. (2018), and only the contours of 20%, 40%, 60%, and 80% maximum power are shown. Dashed black lines indicate the trench. Thin gray contours show the Slab2.0 model (Hayes et al., 2018). The purple contours in (a) show the 20 m and 50 m of coseismic slip distribution during the 2011 Tohoku earthquake from Lay et al. (2012), and the black solid line shows the location of the velocity profile of Miura et al. (2005). (d) Centroid depths of the low-frequency (0.05 - 0.25 Hz) BP images compared with the high-frequency (0.25 - 1 Hz) BP images from 245 M > 6.5 earthquakes.

pared to the footwall materials. This particular structure tends to trap seismic waves within the wedge and cause significant dynamic stress perturbations (Brune, 1996; Nielsen, 1998; Oglesby et al., 2000; Ma & Beroza, 2008; Guo et al., 2016; Gabuchian et al., 2017; Tal et al., 2020). Such high stresses can lead to material yielding (Ma & Hirakawa, 2013; Ma & Nie, 2019) or unclamping and flapping of the hanging wall (Brune, 1996; Gabuchian et al., 2017; Tal et al., 2020).

This study evaluates the impact of the free surface and a realistic, elastic subduction-zone structure on the rupture dynamics and seismic radiation of megathrust earthquakes. We use two-dimensional (2D) dynamic models to investigate these earthquakes' radiation styles in a realistic Earth structure. A similar exercise was undertaken by Lotto et al. (2017, 2018), albeit a simplification of the 2D elastic structure and a focus on tsunamigenesis. Instead, this contribution uses a tomography-derived elastic model, a realistic model of the shear wavespeed ($V_S$), and provides a comprehensive analysis of the seismic waves generated by these ruptures. Regardless of the modeling settings, all simulations can explain the observations: HF seismic waves are more efficiently generated at depth, LF seismic waves are more efficiently generated near the trench. Therefore, the Earth free-surface effects on waves and ruptures are sufficient to reproduce the observed depth-frequency relation.

Furthermore, realistic Earth models amplify the difference in radiation style. The subduction of a cold hydrated slab produces a strong material contrast across the plate interface or fault, which favors the evolution of self-healing rupture front and enhances high-frequency strong ground motions from the downdip region that is near the coast. We conclude that modeling earthquake with a realistic Earth is necessary to predict better tsunami and coastal ground motion hazards.

## 2 Methods

We perform dynamic rupture modeling in 2D media. We gradually increase structural complexity from homogeneous to realistic elastic structures and from small to large earthquakes. We then analyze the spectral properties of the rupture slip history, the nearby ground motions, and the tsunami potential.

### 2.1 Representing a realistic megathrust structure

We choose the Tohoku region in northeastern Japan as our study case. We increase the complexity of the medium from a homogeneous half-space with a planar shallow dipping fault (11.8° degrees, Fig. 2a) to a heterogeneous half-space with realistic geometry and a regional $V_P$ structure from Miura et al. (2005) (Fig. 1a and Fig. 2b). The elastic structure varies considerably along the dip of the megathrust, especially $V_P$ in the upper plate (Sallarès & Ranero, 2019). Another aspect of the structural complexity is the high compliance of the sediments that constitute the accretionary wedge (Von Huene et al. (2009), and references therein). Here, we describe the megathrust fault zone into two canonical fault zone structures: 1) the updip fault zone has low-velocity properties and high $V_P/V_S$ ratio, a nearby free surface, and a wide damaged zone, and 2) the downdip fault zone has a sharp contrast in material properties across the fault.

We focus our efforts to model a realistic updip region (above 20 km) on generating a realistic $V_S$ structure. The compilation of $V_P/V_S$ ratio values provided by Brocher (2005) suggests that low $V_P$ materials have high $V_P/V_S$ ratios. In light of this, we discuss three regions of possibly elevated $V_P/V_S$ ratios. The first region is the subduction channel, the thin upper layer of the downgoing slab that is composed of fluid-rich seafloor sediments (Naif et al., 2015; Saffer & Tobin, 2011; Zhu et al., 2020) and hydrated minerals in a mafic fractured crust (Shelly et al., 2006; Hicks et al., 2014; Bostock, 2013; Nishimura et al., 2019; Pimienta et al., 2018). The second region is the slope apron, the thin layer of the seafloor sediments that covers the wedge, which is best accessed by offshore drilling and active seismic surveys (Peacock et al., 2010; Tsuji et al., 2011; Fujie et al., 2013; Zhu et al., 2020). The third region we consider is the frontal prism that is the tip of the accretionary wedge where dragging of high $V_P/V_S$ ratio sediments may occur (Saffer & Tobin, 2011; Fujie et al., 2013; Nakamura et al., 2014). Due to the range of $V_P/V_S$ values found in the literature, we vary the ratios between $\sqrt{3}\sim$1.73, 1.83, 1.94, 2.04, 2.14, 2.24, 2.35, and 2.45 in the three specific regions discussed above (Fig. S6). Although higher values have been reported within layers of seafloor sediments (Zhu et al., 2020), these are likely too thin to be resolved by our numerical exercise.

We now focus our attention on modeling material contrasts at the plate interface in the downdip region (between 20 and 50 km depth). Although the downgoing oceanic

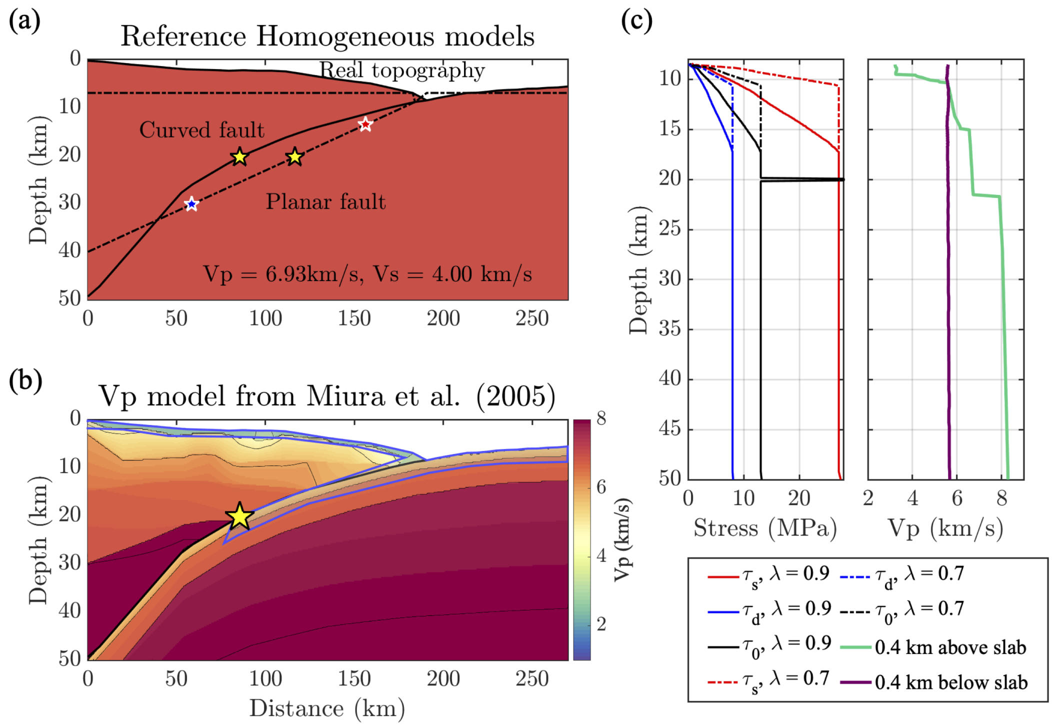


**Figure 2. Model setting**. (a) Model configuration in the homogeneous structure: flat half-space with planar slab/fault geometry and flat topography (dashed lines), a half-space with realistic slab geometry and seafloor topography (solid lines, referred to later as REF), hypocentral locations (yellow for the large ruptures, red and blue for the partial ruptures). (b) Heterogeneous half-space with realistic seafloor topography and V$_P$ structure from Miura et al. (2005). (c) Fault properties: static strength levels $\tau_s$ (red), dynamic strength levels $\tau_d$ (blue), initial shear stress $\tau_0$ (black) with different values of pore-pressure ratio $\lambda$ of 0.7 (dashed lines) and 0.9 (solid lines), V$_P$ along with two profiles projected at 400-m above (green) and 400-m below the plate interface (purple).

plate is denser than the overriding plate, the several-kilometer thin upper portion of the oceanic crust exhibits low seismic velocities. It is present in most subduction zones and is referred to as a Low-Velocity Zone (LVZ). To confirm this common feature of subduction zones, we compile the range of V$_P$ in the LVZ and across the fault in the upper plate in Supplementary Materials Table S1.

Finally, we embed the realistic structure in a homogeneous half-space and generate a larger simulation domain to avoid artifacts from the absorbing boundary conditions. We impose a 5-km smoothing operator to taper off velocity changes between the realistic structural model and the homogeneous half-space (Supporting Information Figure S7). Later benchmark cases also use a homogeneous full-space.

### 2.2 Modeling the dynamic rupture

The other ingredients necessary to model earthquake ruptures are fault properties such as the stress field, the pore pressure, and the frictional conditions (Fig. 2c). We explore several frictional conditions. In most models, we apply linear slip weakening on the entire fault. We test for slip-neutral and slip-strengthening conditions in the upper $\sim$ 10 km of the along with-dip direction, in a zone of low-grade metamorphism where neutrally stable conditions may occur (Huang et al., 2012; Kozdon et al., 2013; Noda & Lapusta, 2013; Lotto et al., 2017, 2018). We also test the frictional constitutive relation proposed by Murphy et al. (2018) that is derived from laboratory experiments. In addition to increasing the $V_P/V_S$ ratio, the fluid content also affects the stress fields by reducing overburden lithostatic pressure $\sigma_L$ with pore fluid pressure $p$. We use the pore pressure ratio $\lambda$ defined in Hubbert and Rubey (1959) to impose a pore pressure $p = \lambda\sigma_L$ as well as the effective normal stress $\bar{\sigma}_n = (1-\lambda)\sigma_L$. Given the uncertainties in $\lambda$, we test two values of $\lambda$ (0.7 and 0.9) and assume that the pore fluid pressure becomes lithostatic ($\lambda = 1$) when $\bar{\sigma}_n = 40$ MPa (Fig. 2d). These conditions are similar to those discussed and imposed in previous studies (e.g., Rice, 1992; Saffer & Tobin, 2011; Murphy et al., 2018; Lotto et al., 2018). The earthquake rupture naturally evolves on the fault in response to an over-stressed nucleation patch (see Fig. 2c). A full description of all model parameters is in Supporting Information (Text S2). We use the SEM2DPACK software ( `http://www.sourceforge.net/projects/sem2d/`, last accessed on 08/30/2019) to simulate both the dynamic slip on the fault and the wavefield in the two-dimensional elastic domain.

### 2.3 Parameterization of the source radiation

To understand the relative contributions between LF and HF seismic waves emitted by the rupture, we parameterize the local slip-rate function's spectrum and improve from the qualitative discussions in Ma and Hirakawa (2013) and Galvez et al. (2014). In this study, we systematically measure and compare the along-dip spectral variations with two metrics.

The first approach fits the Fourier amplitude spectrum of the local slip-rate function with a flat model at low frequencies and a power-law decay at high frequencies. We apply a model commonly used in source seismology, $S(f) = 1/\left(1 + (f/f_c)^n\right)$, where $f_c$ and $n$ are the corner frequency and spectral falloff rate, respectively. The spectral model fits the shape of far-field P-wave pulses that originate from circular crack ruptures with uniform stress drop and elliptical slip distribution (Eshelby, 1957; Brune, 1970; Madariaga, 1976). It is common to perform spectral fitting over the spectrum of the far-field body-wave pulse of the entire event (Abercrombie & Rice, 2005; Allmann & Shearer, 2009; Trugman & Shearer, 2017; W. Wang & Shearer, 2019). While it is not an appropriate model for asymmetric surface-rupturing events, we use this spectral shape to characterize the spectral content. We apply a non-linear least-square solver to find $f_c$ and $n$ from fitting the $\log_{10}$ of the amplitude spectra of the local slip-rate functions interpolated on a logspace frequency vector, a strategy similar to other observational studies (see Shearer et al. (2019) for a recent review). The corner frequency $f_c$ is inversely proportional to the pulse duration, which is also referred to as "rise time" in the source function's kinematic representation. The spectral falloff rate $n$ describes how fast the high-frequency component decays in amplitude. The combination of both parameters can help quantify the relative portions of LF and HF seismic radiation. They tradeoff each other during the spectral fit (Denolle & Shearer, 2016; Trugman & Shearer, 2017), and both quantify the high-frequency contribution: larger $f_c$ and smaller $n$ correspond to relatively more HF radiation, while smaller $f_c$ and larger $n$ correspond to relatively more LF radiation.

The second measure of relative contribution in frequency content estimates the seismic power generated by the local slip-acceleration function. We estimate the power by bandpassing (Butterworth, four corners, zero phase) and integrating the time series of local slip-acceleration functions in two frequency bands below the resolvable frequency: for partial rupture in the homogeneous medium (section 3.1), LF 0.001-0.05 Hz and HF 0.05 - 2 Hz; for full rupture (section 3.2), LF 0.001-0.06 Hz and HF 0.06 - 0.3 Hz. Details about the frequency resolution are in the Supporting Materials (Text S2.4). We then use the HF and LF seismic powers, specifically the HF/LF power ratio, to measure their relative contributions.

# 3 Results from dynamic rupture simulation of megathrust earthquakes

## 3.1 Cases of partial ruptures

We start by inquiring whether the model setup can reproduce the differences in pulse width and fall-off rate that are reported from observations of moderate-size subduction-zone events (Houston, 2001; Ye et al., 2016). We model two small ruptures in a simple structure of a planar fault and flat-free surface (Fig. 2a). We impose pre-stress conditions to constrain the rupture length but keep all other parameters equal for both simulations (see Fig. S8). Any difference in rupture style may then be attributed to the depth (or distance from the free surface) at which the rupture occurs. The shallow rupture reaches the trench and interacts with the scattered wavefields. Such wave interaction does not happen for the deep source as the rupture ends before the arrival of free-surface reflections; the deep source is effectively in a full-space. The simulations show that the shallow rupture ends up releasing about twice the moment (per unit of fault width) as the deep rupture (i.e., twice as large, Fig. 3a).

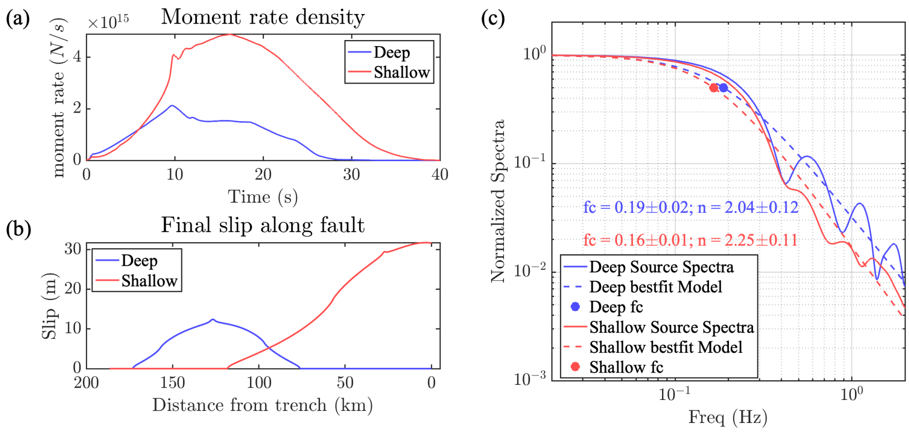


**Figure 3. Simulating a shallow and a deep moderate-size megathrust earthquake.** (a) Slip-rate functions averaged over the entire fault; (b) Final slip distributions on fault; (c) Amplitude-normalized source spectra of the two earthquakes (solid lines) as well as their corresponding best-fitted spectral models (dashed lines). The dots indicate the values of corner frequency $f_c$.

Next, we fit the overall moment-density-rate function with the spectral model within the resolvable frequency band below 2 Hz (Fig. 3c). This is in practice very similar to the seismological studies that explore earthquake source parameters such as stress drop and radiated energy (e.g., Abercrombie & Rice, 2005; Baltay et al., 2014; Denolle & Shearer, 2016; Trugman & Shearer, 2017). The spectral analysis shows that the source spectrum of the shallow earthquake has lower $f_c = 0.16$ Hz and higher $n = 2.25$ than the deep earthquake with $f_c = 0.19$ Hz and $n = 2.04$ (Fig. 3c). We expect $f_c$ to be lower given that the shallow rupture lasts longer and that the overall moment is greater. The stress drop is the same for both events by the construction of this dynamic model. The difference in corner frequency and moment does not follow the usual moment duration scaling expected for self-similar ruptures ($\mathrm{M}_0 \sim f_c^{-3}$), which probably stems from the difference between two-dimensional (2D) and three-dimensional (3D) models and because the shallow rupture does not have the same slip-profile as the deep rupture (Fig. 3b).

We also calculate the ratio of seismic power in an LF band (here 0.001 - 0.05 Hz, well below the event corner frequencies) and an HF band (here 0.05 - 2 Hz), as described above. The corresponding HF/LF ratio of shallow rupture is 0.771, while the deep rupture ratio is 1.024. This second metric reaffirms that meaning that HF than the deep rupture.

### 3.2 Cases of full ruptures

Our half-space simulations are typical of 2D models of dynamic rupture (Huang et al., 2012; Kozdon et al., 2013; Lotto et al., 2017; Ramos & Huang, 2019). All simulated ruptures reach the trench, last about 60 seconds, and their final slip increases from small downdip to large updip. Examples of the space-time evolution of the ruptures are shown in Figure 4a. The rupture first propagates bilaterally from its nucleation patch. The updip rupture then hits the trench with a high slip-rate, and a weak re-rupture front propagates back downdip. The downdip rupture propagates with a constant rupture velocity and dies at the end of the fault. The slip profiles along the dip (Fig. 5) are similar to the ones inferred for the Mw 9.0 2011 Tohoku-oki earthquake (Ide et al., 2011; Simons et al., 2011; K. Wang et al., 2018).

By comparison, the simulation that ran in the homogeneous full-space model presents symmetric rupture behavior at the updip and downdip propagating fronts. The slight difference is due to the initial stress distribution (Fig. 4a and Fig. 5b). We refer to Supporting Information 2 for each model's detailed results and only summarize here their general patterns. To explore the depth-varying properties, we select an individual slip-rate function every 10 km along with the plate interface and measure its frequency content (Fig. 6). We also repeat the measurements for the segment-averaged slip-rate functions, and the results do not affect our conclusions (Fig. S9).

First, we perform the spectral fitting for each slip-rate function. We find that all models with a free surface present similar along-dip (or depth) variations of the spectral properties (Fig. 6a and Fig. S9). The spectral falloff rate $n$ generally decreases with depth: it is about 1.8 - 2.0 (model median) on the shallow segment from 0 - 20 km and 0.8 - 1.0 (model median) on the deep segment.

Second, we calculate the power ratio of slip accelerations in the HF (0.06 - 0.3 Hz) and LF (0.001 - 0.06 Hz) bands. The central frequency 0.06 Hz is arbitrarily chosen as the middle of the log-scale frequency band, but other tested values did not affect the results. We choose slip acceleration as the ground motion unit because far-field velocity seismograms are commonly used for teleseismic P-wave back-projection studies (Fukahata et al., 2014b; Yin & Denolle, 2019) and are proportional to moment accelerations. Here again, we find a clear pattern that the HF/LF power ratio increases with depth (downdip) for all those half-space models (Fig. 6b).

In all free-surface models, both measures of the local slip-rate functions' relative frequency content vary systematically with depth. Such systematic variation contrasts with the results obtained with the full-space model's case: both the spectral falloff rate $n$ and the HF/LF ratio remain constant (Fig. 6). This suggests that the free-surface effects are sufficient to explain the frequency-depth radiation in megathrust earthquakes.

## 4 Discussion

This study focuses on the effects of a realistic Earth structure on the dynamic rupture behavior of megathrust earthquakes. While we test one particular subduction zone in northeastern Japan (Miura et al., 2005), the overall structure exists in many other subduction zones (Table S1). Three specific structural features appear to impact the depth-frequency relation of megathrust earthquakes (Fig. 7): 1) the free surface in the near-source region, 2) the high compliance of the sediments in the updip wedge, and 3) the low-velocity zone below the plate interface downdip. The free-surface effects are the dom-

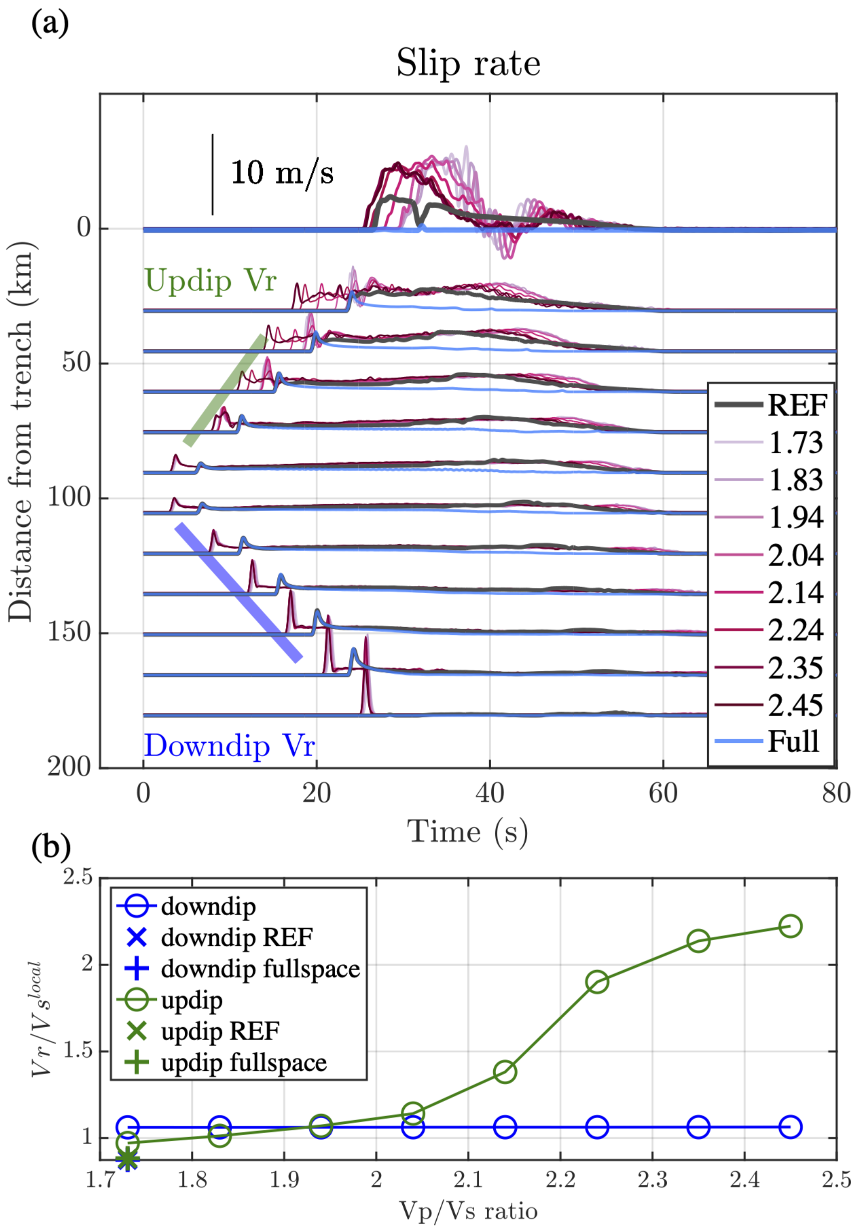


**Figure 4. Space time evolution of the simulated megathrust earthquake.** Comparisons of simulation results with $\lambda = 0.9$ from different values of $V_P/V_S$ ratio under model settings (Fig. 2b) and homogeneous models: REF model with real topography in Figure 2a (dark gray) and full-space model (light blue). (a) Space-time slip-rate evolution: green and blue lines crudely mark the updip and downdip rupture front. (b) Rupture speeds of updip (in green, 40 km to 80 km from the trench) and downdip (in blue, 110 km to 160 km from the trench) propagation for each model.

inant factor, but the heterogeneity in material compliance further enhances the radiation contrast. We illustrate this in Figure 7. Next, we discuss the rupture behavior and

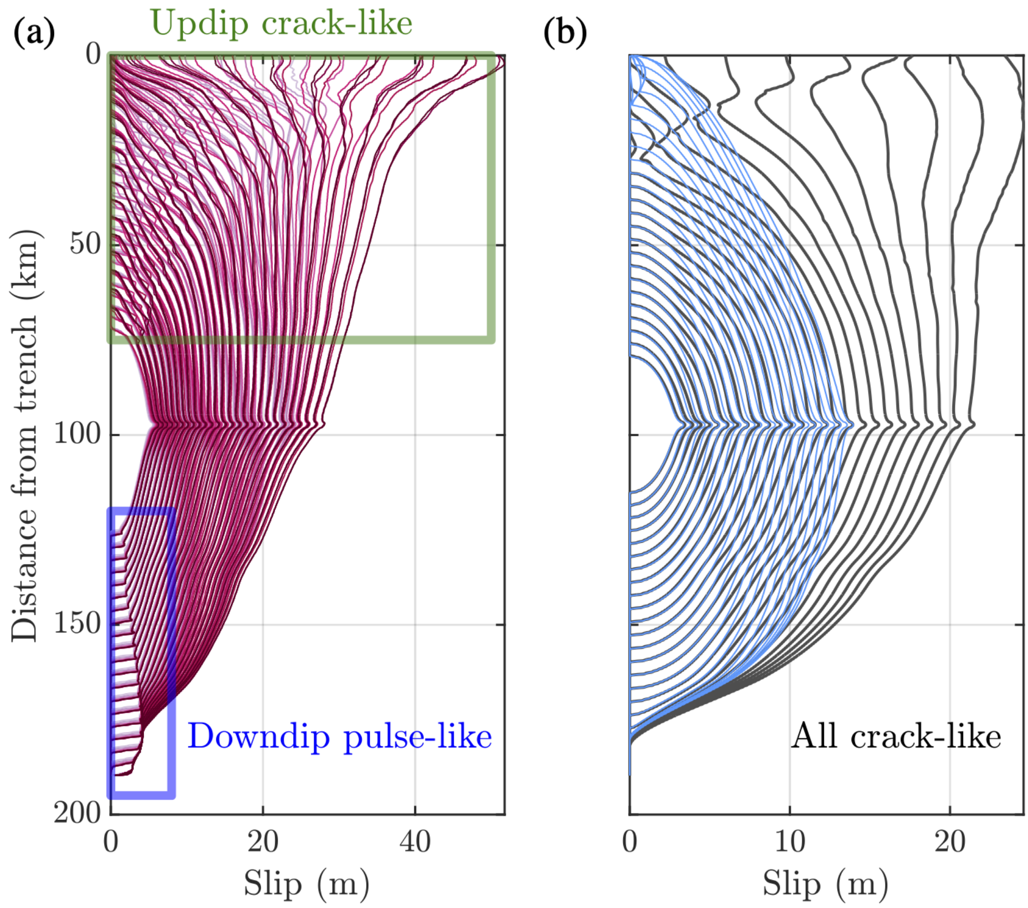


**Figure 5. Slip history of the simulated earthquakes.** Snapshots of slip distribution from (a) models with heterogeneous velocity structures and different $V_P/V_S$ ratios; (b) homogeneous models in half-space with real topography (dark gray) and in full-space (blue). Slip contours from every second between 10 to 35 s are plotted.

further argue that a realistic structure is necessary for better seismic and tsunami hazard assessment.

### 4.1 Updip rupture: large and fast crack rupture to the trench

The rupture accelerates updip and evolves in a crack-like mode (Fig. 5): the shallow rupture velocities are higher than typically observed (Chounet et al., 2018) and greater than the surrounding $V_S$, and slip continues until the end of rupture. Our simulations shed light on two major factors that control this updip behavior: the free surface and the shallow compliant fault zone.

Previous studies have shown that the free surface can significantly change the normal stress during rupture, due to waves reflecting at the free surface and traveling back to the fault (Brune, 1996; Nielsen, 1998; Oglesby et al., 1998, 2000; Y. Wang et al., 2019; Tal et al., 2020). Our simulation results are no different: clear surface-reflected phases cause the prolonged and persistent slip in the updip portion (Supporting Information 2). Free-surface effects also induce acceleration of rupture propagation with supershear velocity, which is also seen in other tectonic regimes such as strike-slip earthquakes (Kaneko & Lapusta, 2010).

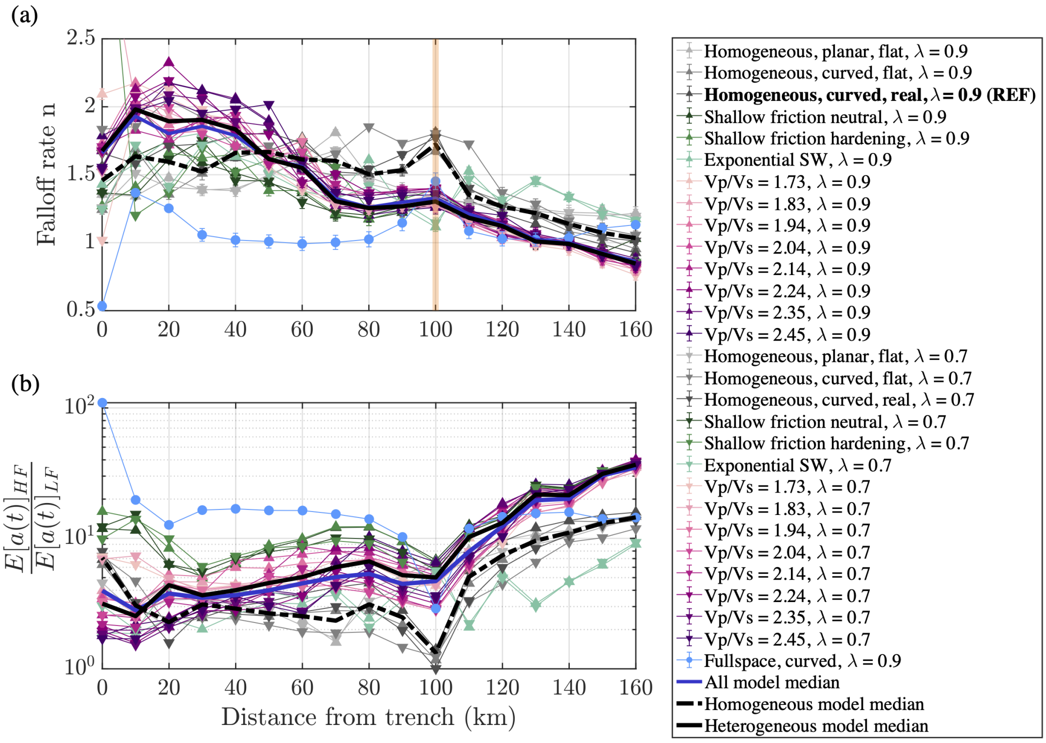


**Figure 6. Spectral properties of the source radiation,** (a) Best-fitted spectral falloff rate $n$ along dip from the simulated megathrust earthquake with different model settings. (b) The power ratio of high frequency (HF) 0.06 - 0.3 Hz and low frequency (LF) 0.001 - 0.06 Hz slip acceleration along dip. Colored lines refer to different models. The yellow bar indicate the location of rupture nucleation.

The highly compliant structure of the shallow hanging wall of the megathrust acts as a seismic waveguide. The upper plate low-velocity sediments can trap seismic waves, amplify their amplitudes and extend their duration. This wave propagation effect is similar to how seismic waves amplify when traveling in sedimentary basins (Campillo et al., 1989). Despite differences in model settings, all simulations show that the initial wave emitted at the rupture front, the free-surface reflections, and other wedge captured and scattered waves interfere together to energize rupture propagation and increase the final slip. In our simulations, these normal stress changes and fault-parallel slip are so extreme, with peak slip rates on the order of 10 m/s, that some models with standard $V_P/V_S$ ratios predict co-seismic backslip (Fig. 4a). In simulations with higher $V_P/V_S$ ratios, much lower $V_S$ may delay the propagation of scattered waves in a way that limits their constructive interference back to the fault. Regardless, such extreme values of slip rates generate large dynamic stresses that can cause (not modeled) inelastic failure (Ma & Hirakawa, 2013; Ma & Nie, 2019), wedge flapping (Brune, 1996; Gabuchian et al., 2017). This phenomenon may be the cause for the suggested dynamic overshoot during the Mw 9.0 2011 Tohoku-oki earthquake (Ide et al., 2011).

The downgoing plate is fractured and hydrated on the foot-wall side with low velocities and elevated $V_P/V_S$ ratios. Altogether, the structure is similar to that observed in crustal damage zones (Ben-Zion & Sammis, 2003). Harris and Day (1997) suggested that the low-velocity structure around the fault can affect the rupture speed and slip-velocity pulse shape. Furthermore, such a low-velocity structure dramatically impacts rupture propagation and termination, such as multiple slip pulses, supershear rupture

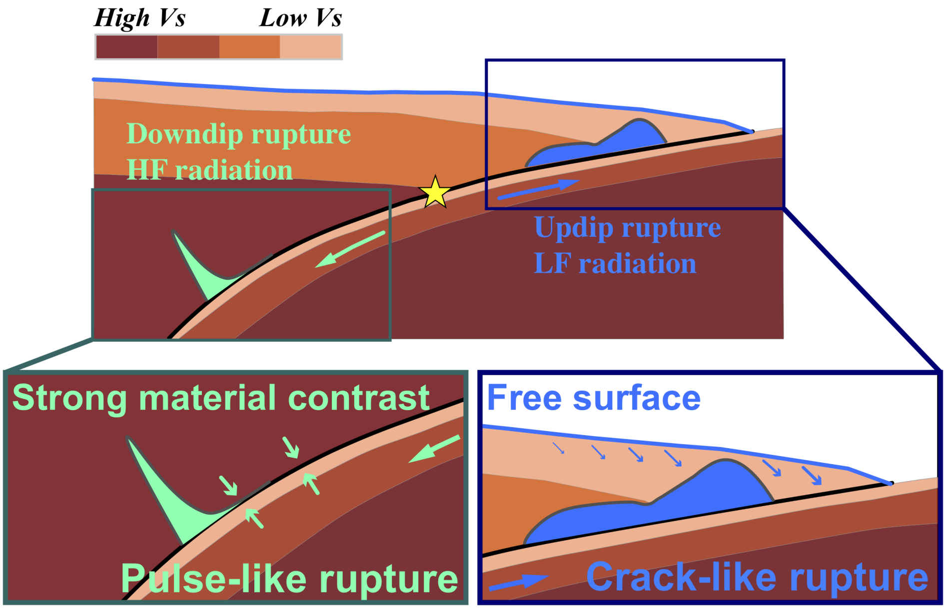


**Figure 7. Effects of the free surface and material contrasts on the dynamic behavior of megathrust earthquakes**. In the updip region, the free surface leads to crack-like rupture and enhanced low-frequency radiation. In the downdip part, the substantial material contrast at the top of the LVZ favors pulse-like rupture and enhanced high-frequency seismic radiation.

velocity, and rotation of background stress (Ampuero & Ben-Zion, 2008; Huang et al., 2014; Huang, 2018).

In the homogeneous case with a uniform $V_P/V_S$ ratio of $\sqrt{3}$ and realistic fault and seafloor geometries (REF model in Fig. 6 and Fig. 8), the rupture velocity for both up and down dip rupture has a typical value of $0.87V_S$. In the models that have realistic $V_P/V_S$ ratios, the updip rupture velocity becomes greater than the local $V_S$. This is typical for 2D elastic models of earthquakes in subduction zone (Lotto et al., 2018) and in damaged fault zones (Huang et al., 2014; Weng et al., 2016; Huang et al., 2016).

### 4.2 Downdip rupture: pulse-like rupture along with the LVZ

As the rupture propagates to the downdip region, there is no impact from free-surface reflections as the rupture heals before waves travel back to the fault. All models present a sharp rupture front (Fig. 4a). In the models with a homogeneous structure, the slip-rate functions have typical decays, and long tails (Kostrov, 1964). In the models with heterogeneous structures, the slip-rate functions are characterized by a shortening of the slip pulse (stronger healing) with depth (or along dip) of the hypocentral distance. In both situations, our quantification on the spectrum shows that the HF energy dominates due to the impulsive slip-rate function shape.

The material contrast can explain the evolution of short and sharp slip pulses in the heterogeneous models at the plate interface downdip of the hypocenter. Shlomai and Fineberg (2016) perform and analyze lab experiments with an in-plane shear of the two blocks with different compliance. They find that such a bimaterial interface can host both rupture modes: one self-healing slip pulse that moves in one direction of rupture and one slip crack that propagates in the opposite direction. The experimental configuration is similar to that of the subduction zones downdip of the seismogenic zone with the contact between the LVZ and the overhanging upper mantle material. As the rupture propagates downdip, in the moving direction of the compliant oceanic plate, the slip-rate functions are short and sharp pulses (Fig. 4a), and the corresponding downdip rupture speed $V_r$ is close to the local $V_S$ of the oceanic crust near the slab (Fig. 4b).

### 4.3 Frequency-depth radiation of megathrust earthquakes

In this study, we have shown that all earthquakes simulated in half-spaces exhibit similar along-dip variations in spectral parameters and HF/LF ratios of the local slip-rate functions (Fig. 3, Figure 6 (a) and (b)), which is consistent with the observed depth-frequency relation (Fig. 1). By contrast, the benchmark full-space simulation is not. Therefore, the free-surface effects are the leading factor in explaining the observed depth-frequency relation of megathrust earthquakes.

The cases of partial ruptures (Fig. 3) reveal that the shallow megathrust earthquakes are more depleted in high-frequency radiation than the deep ones. These patterns are consistent with the observed systematic depth variations of source parameters for small-to-moderate earthquakes(Houston, 2001; Ko & Kuo, 2016; Denolle & Shearer, 2016; Ye et al., 2016).

The cases of full ruptures also reveal that the deep portion of the rupture has elevated high-frequency radiation compared to the shallow part of the rupture. We now draw attention to the BP results showing a depth-frequency relation during individual megathrust earthquakes (see details in the introduction). Our study suggests that a crack-like rupture mode exemplifies the updip rupture of megathrust earthquakes, whereas the self-healing of slip pulses is typical of downdip ruptures. The parameterization of the slip-rate functions in the spectral domain (Figs. 6a and b) validates that the different rupture modes can explain the depth-frequency relation: i) in the updip region, the rupture radiates more efficiently LF seismic waves due to the interference of waves and rupture in a complex structure, ii) in the downdip part, the rupture radiates more efficiently HF seismic waves due to the strong material contrast from LVZ and continental mantle.

Furthermore, we notice that the models that include realistic velocity structures (Fig. 6b) tend to present enhanced depth variations of the radiation spectral content, with larger differences in values of falloff rate $n$ and HF/LF ratios. Therefore, the compliance of shallow materials is another controlling factor to the depth-varying frequency-dependence of seismic radiation.

### 4.4 Implications for tsunami and ground motion hazards

Our simulations indicate that the final slip distribution varies considerably with the model settings. The final moment magnitude of the homogeneous half-space models is larger than the heterogeneous models, probably due to the greater shear modulus at the shallow portion (Fig. 8a). However, the final slip is greater underneath shallow and highly compliant structures (Fig.8b), which was also found by Lotto et al. (2018). The final slip at the trench directly impacts the tsunami height. We apply a simplified relation from Tanioka and Satake (1996) to estimate the initial tsunami height at the trench: $\eta_{ts} = u_y - m u_x$, where $u_x$, $u_y$, and $m = -0.1$ are the horizontal displacement, vertical displacement, and the horizontal gradient of the bathymetry at the trench, respectively. We find that $\eta_{ts} = 8.6$ m for the homogeneous half-space model (REF model), 11.0 m for the heterogeneous model with $V_P/V_S = \sqrt{3}$ and 11.3 m for the heterogeneous model with $V_P/V_S = 2.45$. This simple exercise reaffirms the results from previous studies that the realistic velocity structure, especially the shallow $V_S$ structure, is necessary to estimate better the potential tsunami hazards (Lotto et al., 2018).

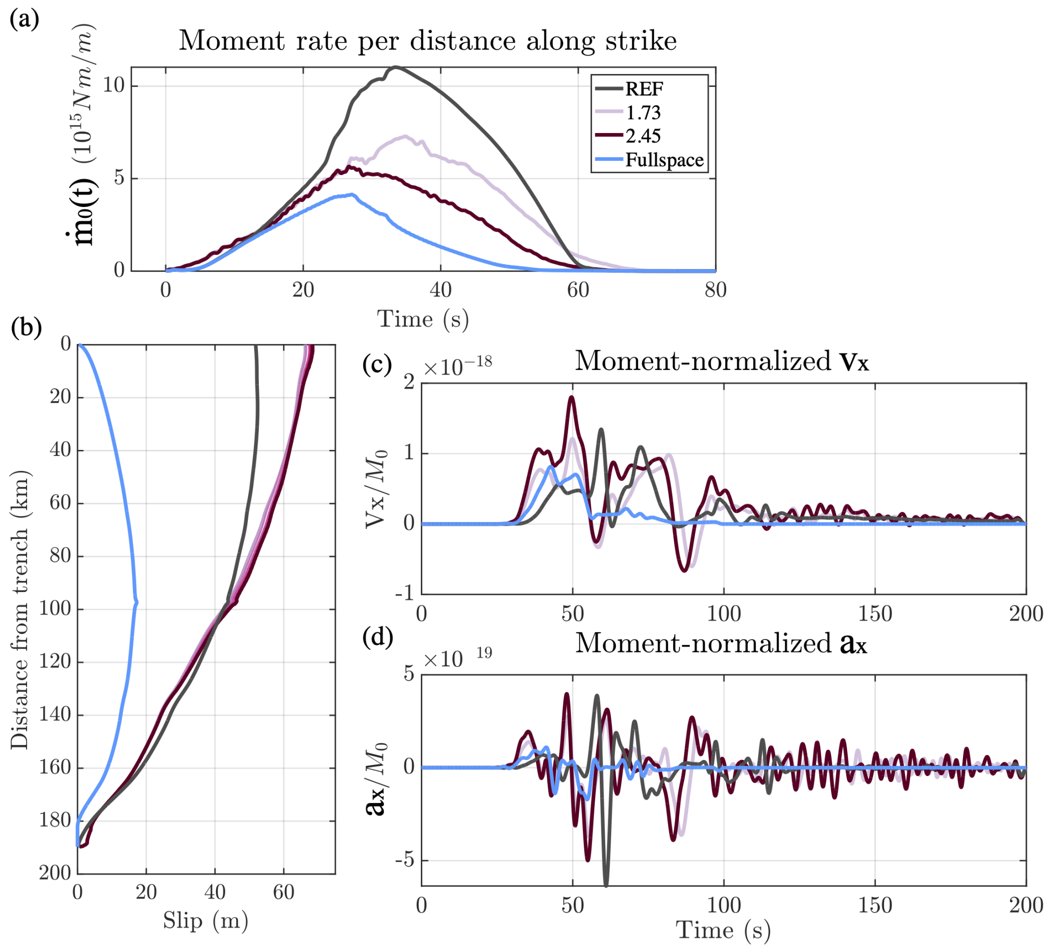


**Figure 8. Tsunami and ground motion hazards.** (a) Moment-rate density function of each model with different $V_P/V_S$ ratios. (b) Final along-dip slip distribution from different models. (c) Moment-normalized velocity seismograms (horizontal x direction) recorded by the far-field station (location shown in Fig. S7b). (d) Corresponding moment-normalized acceleration seismograms (horizontal x-direction) recorded by the same virtual station.

We also compare the ground motions that would be recorded at a station in the coastal region (Fig. 8c-d). The strong ground motions that are responsible for damaging urban infrastructure may arrive as distinct high-frequency bursts from the downdip part of the megathrust (Kurahashi & Irikura, 2011; Asano & Iwata, 2012; Frankel, 2013). Moment-normalized velocity and acceleration seismograms produced by the different models of this study have relatively similar peak amplitudes. The earliest peak amplitudes of ground motions occur when the rupture hits the trench. However, the duration of strong shaking is much greater in realistic structures. We attribute this to the wave reverberation in the wedge (wave propagation effects) and not a source effect since the source duration is comparable ($\sim$ 60 s). The presence of the LVZ naturally increases the strong ground motion hazard: it is located nearby the coastal regions and tends to produce three times more HF seismic power than in reference, uniform models (Fig.6). Previous studies have illustrated the existence of distinct strong-motion generation areas (SMGAs) (Kurahashi & Irikura, 2011; Asano & Iwata, 2012; Frankel, 2013). The SMGAs imply that there may be heterogeneity in the LVZ such that the spatial variations in elastic structure may control variations in slip-front healing (i.e., more or less healing of the slip pulse). These can also be modeled by heterogeneity in fault properties (Huang et al., 2012).

## 5 Conclusion

Global databases of BP images show a systematic depth variation of the source radiation frequency content. While this finding was discussed in Lay et al. (2012) for several large events, here we show that it is a systematic pattern among most moderate-to-large subduction-zone earthquakes. This study aims to explain this observation. We find that realistic Earth structures, including the Earth's surface, are necessary and sufficient to explain this ubiquitous observation. Here, we argue that the dynamics of shallow rupture are dominated by free-surface effects that are, in turn, the first leading factor in explaining the depth-frequency relation. The second-order effect is the evolution of earthquake rupture in a structure that is typical of shallow subduction zones, one that has a compliant wedge and a low-velocity zone atop the downgoing slab. The presence of anomalously low $V_S$, relative to $V_P$, also impacts the rupture behavior that further exacerbates the radiation's depth-dependence.

Our findings resonate with previous work that realistic structures are necessary to correctly model tsunami and ground motion hazards in future subduction zone earthquakes (Lotto et al., 2018). Because elastic wavespeed properties are likely better constrained than frictional properties at depth, our study promotes the use of tomographic images in dynamic rupture modeling and ground motion predictions. Our simulations do not include inelastic rheology, which can predict greater tsunami hazards (Ma & Hirakawa, 2013; Ma & Nie, 2019) and affect on-fault rupture propagation and far-field radiation. More realistic Earth structure and material rheological properties are essential research directions to predict better earthquake behavior, tsunami, and ground-motion hazards.

**Acknowledgments**

We sincerely thank Seiichi Miura at JAMSTEC (Japan Agency for Marine-Earth Science and Technology) for providing the velocity model of the Japan trench. We are grateful to Yihe Huang and Alice-Agnes Gabriel for constructive and productive discussions. We are grateful to Jean-Paul Ampuero for developing SEM2DPACK (available at `http://www.sourceforge.net/projects/sem2d/`). The back-projection results used in Figure 1 (a) are downloaded from IRIS data services products: back-projection (`https://ds.iris.edu/ds/products/back-projection/`, last accessed on 02/27/2021). The Slab2.0 model is downloaded from U.S. Geological Survey (`https://www.sciencebase.gov/catalog/item/5aa1b00ee4b0b1c392e86467`, last accessed on 02/27/2021). All the down-sampled simulation results and relevant scripts are in Figshare (`https://figshare.com/projects/The_Earth_surface_controls_the_depth-dependent_seismic_radiation_of_megathrust_earthquakes/98360`) for result reproduction. This work is supported by the CAREER EAR-1749556 NSF award).

## References

Abercrombie, R. E., & Rice, J. R. (2005). Can observations of earthquake scaling constrain slip weakening? *Geophysical Journal International*, *162*(2), 406–424. doi: 10.1111/j.1365-246X.2005.02579.x

Allmann, B. P., & Shearer, P. M. (2009). Global variations of stress drop for moderate to large earthquakes. *Journal of Geophysical Research: Solid Earth*, *114*(B1), B01310. doi: 10.1029/2008JB005821

Ammon, C. J., Kanamori, H., & Lay, T. (2008). A great earthquake doublet and seismic stress transfer cycle in the central Kuril islands. *Nature*, *451*(7178), 561–565. doi: 10.1038/nature06521

Ampuero, J.-P., & Ben-Zion, Y. (2008). Cracks, pulses and macroscopic asymmetry of dynamic rupture on a bimaterial interface with velocity-weakening friction. *Geophysical Journal International*, *173*(2), 674–692. doi: 10.1111/j.1365-246X.2008.03736.x

Asano, K., & Iwata, T. (2012). Source model for strong ground motion generation in the frequency range 0.1–10 Hz during the 2011 Tohoku earthquake. *Earth, Planets and Space*, *64*(12), 6. doi: 10.5047/eps.2012.05.003

Avouac, J.-P., Meng, L., Wei, S., Wang, T., & Ampuero, J.-P. (2015). Lower edge of locked Main Himalayan Thrust unzipped by the 2015 Gorkha earthquake. *Nature Geoscience*, *8*(9), 708–711. doi: 10.1038/ngeo2518

Baltay, A. S., Beroza, G. C., & Ide, S. (2014). Radiated Energy of Great Earthquakes from Teleseismic Empirical Green's Function Deconvolution. *Pure and Applied Geophysics*, *171*(10), 2841–2862. doi: 10.1007/s00024-014-0804-0

Ben-Zion, Y., & Sammis, C. G. (2003). Characterization of fault zones. *Pure and applied geophysics*, *160*(3), 677–715.

Bilek, S. L., & Lay, T. (1999). Rigidity variations with depth along interplate megathrust faults in subduction zones. *Nature*, *400*(6743), 443–446.

Bostock, M. G. (2013). The Moho in subduction zones. *Tectonophysics*, *609*, 547–557. doi: 10.1016/j.tecto.2012.07.007

Brocher, T. M. (2005, 12). Empirical Relations between Elastic Wavespeeds and Density in the Earth's Crust. *Bulletin of the Seismological Society of America*, *95*(6), 2081-2092. doi: 10.1785/0120050077

Brune, J. N. (1970). Tectonic stress and the spectra of seismic shear waves from earthquakes. *Journal of Geophysical Research*, *75*(26), 4997–5009. doi: 10.1029/JB075i026p04997

Brune, J. N. (1996). Particle motions in a physical model of shallow angle thrust faulting. *Proceedings of the Indian Academy of Sciences - Earth and Planetary Sciences*, *105*(2), 197. doi: 10.1007/BF02876014

Campillo, M., Gariel, J., Aki, K., & Sanchez-Sesma, F. (1989). Destructive strong ground motion in mexico city: Source, path, and site effects during great 1985 michoacán earthquake. *Bulletin of the Seismological Society of America*, *79*(6), 1718–1735.

Chounet, A., & Vallée, M. (2018). Global and interregion characterization of subduction interface earthquakes derived from source time functions properties. *Journal of Geophysical Research: Solid Earth*, *123*(7), 5831–5852.

Chounet, A., Vallée, M., Causse, M., & Courboulex, F. (2018). Global catalog of earthquake rupture velocities shows anticorrelation between stress drop and rupture velocity. *Tectonophysics*, *733*, 148–158. doi: 10.1016/j.tecto.2017.11.005

Denolle, M. A., & Shearer, P. M. (2016). New perspectives on self-similarity for shallow thrust earthquakes. *Journal of Geophysical Research: Solid Earth*, *121*(9), 2016JB013105. doi: 10.1002/2016JB013105

Eshelby, J. D. (1957). The determination of the elastic field of an ellipsoidal inclusion, and related problems. , *241*, 376–396.

Frankel, A. (2013). Rupture History of the 2011 M 9 Tohoku Japan Earthquake Determined from Strong-Motion and High-Rate GPS Recordings: Subevents Radiating Energy in Different Frequency BandsRupture History of the 2011 M 9 Tohoku Earthquake from Strong-Motion and High-Rate GPS Recordings. *Bulletin of the Seismological Society of America*, *103*(2B), 1290–1306. doi: 10.1785/0120120148

Fujie, G., Kodaira, S., Yamashita, M., Sato, T., Takahashi, T., & Takahashi, N. (2013). Systematic changes in the incoming plate structure at the Kuril trench. *Geophysical Research Letters*, *40*(1), 88–93. doi: https://doi.org/10.1029/2012GL054340

Fukahata, Y., Yagi, Y., & Rivera, L. (2014a). Theoretical relationship between back-projection imaging and classical linear inverse solutions. *Geophysical Journal International*, *196*(1), 552–559. doi: 10.1093/gji/ggt392

Fukahata, Y., Yagi, Y., & Rivera, L. (2014b). Theoretical relationship between back-projection imaging and classical linear inverse solutions. *Geophysical Journal International*, *196*(1), 552–559.

Gabuchian, V., Rosakis, A. J., Bhat, H. S., Madariaga, R., & Kanamori, H. (2017). Experimental evidence that thrust earthquake ruptures might open faults. *Nature*, *545*(7654), 336–339.

Galvez, P., Ampuero, J.-P., Dalguer, L. A., Somala, S. N., & Nissen-Meyer, T. (2014). Dynamic earthquake rupture modelled with an unstructured 3-D spectral element method applied to the 2011 M9 Tohoku earthquake. *Geophysical Journal International*, *198*(2), 1222–1240. doi: 10.1093/gji/ggu203

Guo, Y., Koketsu, K., & Miyake, H. (2016). Propagation mechanism of long-period ground motions for offshore earthquakes along the nankai trough: Effects of the accretionary wedge. *Bulletin of the Seismological Society of America*, *106*(3), 1176–1197.

Harris, R. A., & Day, S. M. (1997). Effects of a low-velocity zone on a dynamic rupture. *Bulletin of the Seismological Society of America*, *87*(5), 1267–1280.

Hayes, G. P., Moore, G. L., Portner, D. E., Hearne, M., Flamme, H., Furtney, M., & Smoczyk, G. M. (2018). Slab2, a comprehensive subduction zone geometry model. *Science*, *362*(6410), 58–61. doi: 10.1126/science.aat4723

Hicks, S. P., Rietbrock, A., Ryder, I. M., Lee, C.-S., & Miller, M. (2014). Anatomy of a megathrust: The 2010 m8. 8 maule, chile earthquake rupture zone imaged using seismic tomography. *Earth and Planetary Science Letters*, *405*, 142–155.

Houston, H. (2001). Influence of depth, focal mechanism, and tectonic setting on the shape and duration of earthquake source time functions. *Journal of Geophysical Research: Solid Earth*, *106*(B6), 11137–11150. doi: 10.1029/2000JB900468

Huang, Y. (2018). Earthquake Rupture in Fault Zones With Along-Strike Material Heterogeneity. *Journal of Geophysical Research: Solid Earth*, *123*(11), 9884–9898. doi: https://doi.org/10.1029/2018JB016354

Huang, Y., Ampuero, J.-P., & Helmberger, D. V. (2014). Earthquake ruptures modulated by waves in damaged fault zones. *Journal of Geophysical Research: Solid Earth*, *119*(4), 3133–3154. doi: 10.1002/2013JB010724

Huang, Y., Ampuero, J.-P., & Helmberger, D. V. (2016). The potential for supershear earthquakes in damaged fault zones–theory and observations. *Earth and Planetary Science Letters*, *433*, 109–115.

Huang, Y., Meng, L., & Ampuero, J.-P. (2012). A dynamic model of the frequency-dependent rupture process of the 2011 Tohoku-Oki earthquake. *Earth, Planets and Space*, *64*(12), 1. doi: 10.5047/eps.2012.05.011

Hubbert, M. K., & Rubey, W. W. (1959). Role of fluid pressure in mechanics of overthrust faulting: I. mechanics of fluid-filled porous solids and its application to overthrust faulting. *GSA Bulletin*, *70*(2), 115–166. doi: 10.1130/0016-7606(1959)70[115:ROFPIM]2.0.CO;2

Ide, S., Baltay, A., & Beroza, G. C. (2011). Shallow dynamic overshoot and energetic deep rupture in the 2011 mw 9.0 tohoku-oki earthquake. *Science*, *332*(6036), 1426–1429.

Incorporated Research Institutions for Seismology Data Management Center. (2011). Data Services Products: BackProjection P-wave back-projection rupture imaging.
doi: 10.17611/DP/BP.1.

Ishii, M., Shearer, P. M., Houston, H., & Vidale, J. E. (2005). Extent, duration and speed of the 2004 Sumatra–Andaman earthquake imaged by the Hi-Net array. *Nature*, *435*(7044), 933. doi: 10.1038/nature03675

Kaneko, Y., & Lapusta, N. (2010). Supershear transition due to a free surface in 3-D simulations of spontaneous dynamic rupture on vertical strike-slip faults. *Tectonophysics*, *493*(3), 272–284. doi: 10.1016/j.tecto.2010.06.015

Kiser, E., Ishii, M., Langmuir, C. H., Shearer, P. M., & Hirose, H. (2011). Insights into the mechanism of intermediate-depth earthquakes from source properties as imaged by back projection of multiple seismic phases. *Journal of Geophysical Research: Solid Earth*, *116*(B6), B06310. doi: 10.1029/2010JB007831

Ko, J. Y.-T., & Kuo, B.-Y. (2016). Low radiation efficiency of the intermediate-depth earthquakes in the Japan subduction zone. *Geophysical Research Letters*, *43*(22), 2016GL070993. doi: 10.1002/2016GL070993

Kostrov, B. V. (1964). Selfsimilar problems of propagation of shear cracks. *Journal of Applied Mathematics and Mechanics*, *28*(5), 1077–1087. doi: 10.1016/0021-8928(64)90010-3

Kozdon, J. E., Dunham, E. M., & Nordström, J. (2013). Simulation of Dynamic Earthquake Ruptures in Complex Geometries Using High-Order Finite Difference Methods. *Journal of Scientific Computing*, *55*(1), 92–124. doi: 10.1007/s10915-012-9624-5

Kurahashi, S., & Irikura, K. (2011). Source model for generating strong ground motions during the 2011 off the Pacific coast of Tohoku Earthquake. *Earth, Planets and Space*, *63*(7), 11. doi: 10.5047/eps.2011.06.044

Lay, T., Kanamori, H., Ammon, C. J., Koper, K. D., Hutko, A. R., Ye, L., … Rushing, T. M. (2012). Depth-varying rupture properties of subduction zone megathrust faults. *Journal of Geophysical Research: Solid Earth*, *117*(B4), B04311. doi: 10.1029/2011JB009133

Lotto, G. C., Dunham, E. M., Jeppson, T. N., & Tobin, H. J. (2017). The effect of compliant prisms on subduction zone earthquakes and tsunamis. *Earth and Planetary Science Letters*, *458*, 213–222. doi: 10.1016/j.epsl.2016.10.050

Lotto, G. C., Jeppson, T. N., & Dunham, E. M. (2018). Fully Coupled Simulations of Megathrust Earthquakes and Tsunamis in the Japan Trench, Nankai Trough, and Cascadia Subduction Zone. *Pure and Applied Geophysics*. doi: 10.1007/s00024-018-1990-y

Ma, S., & Beroza, G. C. (2008). Rupture Dynamics on a Bimaterial Interface for Dipping FaultsRupture Dynamics on a Bimaterial Interface for Dipping Faults. *Bulletin of the Seismological Society of America*, *98*(4), 1642–1658. doi: 10.1785/0120070201

Ma, S., & Hirakawa, E. T. (2013). Dynamic wedge failure reveals anomalous energy radiation of shallow subduction earthquakes. *Earth and Planetary Science Letters*, *375*, 113–122. doi: 10.1016/j.epsl.2013.05.016

Ma, S., & Nie, S. (2019). Dynamic wedge failure and along-arc variations of tsunamigenesis in the japan trench margin. *Geophysical Research Letters*, *46*(15), 8782-8790. doi: 10.1029/2019GL083148

Madariaga, R. (1976). Dynamics of an expanding circular fault. *Bulletin of the Seismological Society of America*, *66*(3), 639–666.

Melgar, D., Fan, W., Riquelme, S., Geng, J., Liang, C., Fuentes, M., … Fielding, E. J. (2016). Slip segmentation and slow rupture to the trench during the 2015, Mw8.3 Illapel, Chile earthquake. *Geophysical Research Letters*, *43*(3), 2015GL067369. doi: 10.1002/2015GL067369

Miura, S., Takahashi, N., Nakanishi, A., Tsuru, T., Kodaira, S., & Kaneda, Y. (2005). Structural characteristics off Miyagi forearc region, the Japan Trench seismogenic zone, deduced from a wide-angle reflection and refraction study. *Tectonophysics*, *407*(3), 165–188. doi: 10.1016/j.tecto.2005.08.001

Murphy, S., Di Toro, G., Romano, F., Scala, A., Lorito, S., Spagnuolo, E., … Nielsen, S. (2018). Tsunamigenic earthquake simulations using experimentally derived friction laws. *Earth and Planetary Science Letters*, *486*, 155–165. doi: 10.1016/j.epsl.2018.01.011

Naif, S., Key, K., Constable, S., & Evans, R. L. (2015). Water-rich bending faults at the Middle America Trench. *Geochemistry, Geophysics, Geosystems*, *16*(8), 2582–2597. doi: 10.1002/2015GC005927

Nakamura, Y., Kodaira, S., Cook, B. J., Jeppson, T., Kasaya, T., Yamamoto, Y., ... Fujie, G. (2014). Seismic imaging and velocity structure around the JFAST drill site in the Japan Trench: low V p, high V p/V s in the transparent frontal prism. *Earth, Planets and Space*, *66*(1), 121. doi: 10.1186/1880-5981-66-121

Nielsen, S. B. (1998). Free surface effects on the propagation of dynamic rupture. *Geophysical Research Letters*, *25*(1), 125–128. doi: 10.1029/97GL03445

Nishimura, K., Uehara, S., & Mizoguchi, K. (2019). An alternative origin of high vp/vs anomalies in slow slip regions: Experimental constraints from the elastic wave velocity evolution of highly fractured rock. *Journal of Geophysical Research: Solid Earth*, *124*(5), 5045–5059.

Noda, H., & Lapusta, N. (2013). Stable creeping fault segments can become destructive as a result of dynamic weakening. *Nature*, *493*(7433), 518–521. doi: 10.1038/nature11703

Oglesby, D. D., Archuleta, R. J., & Nielsen, S. B. (1998). Earthquakes on Dipping Faults: The Effects of Broken Symmetry. *Science*, *280*(5366), 1055–1059. doi: 10.1126/science.280.5366.1055

Oglesby, D. D., Archuleta, R. J., & Nielsen, S. B. (2000). Dynamics of dip-slip faulting: Explorations in two dimensions. *Journal of Geophysical Research: Solid Earth*, *105*(B6), 13643–13653.

Peacock, S., Westbrook, G. K., & Bais, G. (2010). S-wave velocities and anisotropy in sediments entering the Nankai subduction zone, offshore Japan. *Geophysical Journal International*, *180*(2), 743–758. doi: 10.1111/j.1365-246X.2009.04430.x

Pimienta, L., Schubnel, A., Violay, M., Fortin, J., Guéguen, Y., & Lyon-Caen, H. (2018). Anomalous vp/vs ratios at seismic frequencies might evidence highly damaged rocks in subduction zones. *Geophysical Research Letters*, *45*(22), 12,210-12,217. doi: https://doi.org/10.1029/2018GL080132

Ramos, M. D., & Huang, Y. (2019). How the Transition Region Along the Cascadia Megathrust Influences Coseismic Behavior: Insights From 2-D Dynamic Rupture Simulations. *Geophysical Research Letters*, *46*(4), 1973–1983. doi: 10.1029/2018GL080812

Rice, J. R. (1992). Chapter 20 Fault Stress States, Pore Pressure Distributions, and the Weakness of the San Andreas Fault. In B. Evans & T.-f. Wong (Eds.), *International Geophysics* (Vol. 51, pp. 475–503). Academic Press. doi: 10.1016/S0074-6142(08)62835-1

Saffer, D. M., & Tobin, H. J. (2011). Hydrogeology and mechanics of subduction zone forearcs: Fluid flow and pore pressure. *Annual Review of Earth and Planetary Sciences*, *39*, 157–186.

Sallarès, V., & Ranero, C. R. (2019). Upper-plate rigidity determines depth-varying rupture behaviour of megathrust earthquakes. *Nature*, *576*(7785). doi: 10.1038/s41586-019-1784-0

Scholz, C. H. (1998). Earthquakes and friction laws. *Nature*, *391*(6662), 37–42. doi: 10.1038/34097

Shearer, P. M., Abercrombie, R. E., Trugman, D. T., & Wang, W. (2019). Comparing egf methods for estimating corner frequency and stress drop from p wave spectra. *Journal of Geophysical Research: Solid Earth*, *124*(4), 3966–3986.

Shelly, D. R., Beroza, G. C., Zhang, H., Thurber, C. H., & Ide, S. (2006). High-resolution subduction zone seismicity and velocity structure beneath Ibaraki Prefecture, Japan. *Journal of Geophysical Research: Solid Earth*, *111*(B6). doi: 10.1029/2005JB004081

Shlomai, H., & Fineberg, J. (2016). The structure of slip-pulses and supershear ruptures driving slip in bimaterial friction. *Nature Communications*, *7*(1). doi: 10.1038/ncomms11787

Simons, M., Minson, S. E., Sladen, A., Ortega, F., Jiang, J., Owen, S. E., ... Webb, F. H. (2011). The 2011 Magnitude 9.0 Tohoku-Oki Earthquake: Mosaicking the Megathrust from Seconds to Centuries. *Science*, *332*(6036), 1421–1425. doi: 10.1126/science.1206731

Sufri, O., Koper, K. D., & Lay, T. (2012). Along-dip seismic radiation segmentation during the 2007 Mw 8.0 Pisco, Peru earthquake. *Geophysical Research Letters*, *39*(8), L08311. doi: 10.1029/2012GL051316

Tal, Y., Rubino, V., Rosakis, A. J., & Lapusta, N. (2020). Illuminating the physics of dynamic friction through laboratory earthquakes on thrust faults. *Proceedings of the National Academy of Sciences*, *117*(35), 21095–21100.

Tanioka, Y., & Satake, K. (1996). Tsunami generation by horizontal displacement of ocean bottom. *Geophysical Research Letters*, *23*(8), 861–864. doi: 10.1029/96GL00736

Trugman, D. T., & Shearer, P. M. (2017). Application of an improved spectral decomposition method to examine earthquake source scaling in Southern California. *Journal of Geophysical Research: Solid Earth*, *122*(4), 2890–2910. doi: https://doi.org/10.1002/2017JB013971

Tsuji, T., Dvorkin, J., Mavko, G., Nakata, N., Matsuoka, T., Nakanishi, A., ... Nishizawa, O. (2011). VP/VS ratio and shear-wave splitting in the Nankai Trough seismogenic zone: Insights into effective stress, pore pressure, and sediment consolidationTsuji et al.VP/VS ratio & S-wave splitting from OBS data. *Geophysics*, *76*(3), WA71–WA82. doi: 10.1190/1.3560018

Vallée, M. (2013). Source time function properties indicate a strain drop independent of earthquake depth and magnitude. *Nature Communications*, *4*, 2606. doi: 10.1038/ncomms3606

Von Huene, R., Ranero, C. R., & Scholl, D. W. (2009). Convergent margin structure in high-quality geophysical images and current kinematic and dynamic models. In *Subduction zone geodynamics* (pp. 137–157). Springer.

Wang, D., & Mori, J. (2011). Frequency-dependent energy radiation and fault coupling for the 2010 Mw8.8 Maule, Chile, and 2011 Mw9.0 Tohoku, Japan, earthquakes. *Geophysical Research Letters*, *38*(22). doi: 10.1029/2011GL049652

Wang, K., Sun, T., Brown, L., Hino, R., Tomita, F., Kido, M., ... Fujiwara, T. (2018). Learning from crustal deformation associated with the M9 2011 Tohoku-oki earthquake. *Geosphere*, *14*(2), 552–571. doi: 10.1130/GES01531.1

Wang, W., & Shearer, P. M. (2019). An improved method to determine coda-q, earthquake magnitude, and site amplification: Theory and application to southern california. *Journal of Geophysical Research: Solid Earth*, *124*(1), 578–598. doi: https://doi.org/10.1029/2018JB015961

Wang, Y., Day, S. M., & Denolle, M. A. (2019). Geometric Controls on Pulse-Like Rupture in a Dynamic Model of the 2015 Gorkha Earthquake. *Journal of Geophysical Research: Solid Earth*, *124*(2), 1544–1568. doi: 10.1029/2018JB016602

Weng, H., Yang, H., Zhang, Z., & Chen, X. (2016). Earthquake rupture extents and coseismic slips promoted by damaged fault zones. *Journal of Geophysical Research: Solid Earth*, *121*(6), 4446–4457. doi: 10.1002/2015JB012713

Yao, H., Gerstoft, P., Shearer, P. M., & Mecklenbräuker, C. (2011). Compressive sensing of the Tohoku-Oki Mw 9.0 earthquake: Frequency-dependent rupture modes. *Geophysical Research Letters*, *38*(20), L20310. doi: 10.1029/2011GL049223

Yao, H., Shearer, P. M., & Gerstoft, P. (2013). Compressive sensing of frequency-dependent seismic radiation from subduction zone megathrust ruptures. *Proceedings of the National Academy of Sciences*, *110*(12), 4512–4517. doi:

10.1073/pnas.1212790110

Ye, L., Lay, T., Kanamori, H., & Rivera, L. (2016). Rupture characteristics of major and great (mw 7.0) megathrust earthquakes from 1990 to 2015: 2. depth dependence. *Journal of Geophysical Research: Solid Earth*, *121*(2), 845–863.

Yin, J., & Denolle, M. A. (2019). Relating teleseismic backprojection images to earthquake kinematics. *Geophysical Journal International*, *217*(2), 729–747. doi: 10.1093/gji/ggz048

Yin, J., Denolle, M. A., & Yao, H. (2018). Spatial and Temporal Evolution of Earthquake Dynamics: Case Study of the Mw 8.3 Illapel Earthquake, Chile. *Journal of Geophysical Research: Solid Earth*, *123*(1), 344–367. doi: 10.1002/2017JB014265

Yin, J., Yang, H., Yao, H., & Weng, H. (2016). Coseismic radiation and stress drop during the 2015 Mw 8.3 Illapel, Chile megathrust earthquake. *Geophysical Research Letters*, *43*(4), 1520–1528. doi: 10.1002/2015GL067381

Yin, J., Yao, H., Yang, H., Qin, W., Jing, L.-Z., & Zhang, H. (2017). Frequency-dependent rupture process, stress change, and seismogenic mechanism of the 25 April 2015 Nepal Gorkha Mw 7.8 earthquake. *SCIENCE CHINA Earth Sciences*, *60*(4), 796–808. doi: 10.1007/s11430-016-9006-0

Yue, H., Simons, M., Duputel, Z., Jiang, J., Fielding, E., Liang, C., … Samsonov, S. V. (2016). Depth varying rupture properties during the 2015 Mw 7.8 Gorkha (Nepal) earthquake. *Tectonophysics*. doi: 10.1016/j.tecto.2016.07.005

Zhu, J., Canales, J. P., Han, S., Carbotte, S. M., Arnulf, A., & Nedimović, M. R. (2020). Vp/vs ratio of incoming sediments off cascadia subduction zone from analysis of controlled-source multicomponent obs records. *Journal of Geophysical Research: Solid Earth*, *125*(6), e2019JB019239.